



Electrospun titania nanofibers segregated by graphene oxide for improved visible light photocatalysis



Li Zhang^{a,b}, Qinghong Zhang^{b,*}, Hongyong Xie^{a,*}, Jiang Guo^c, Hailong Lyu^c, Yaogang Li^b, Zhiguo Sun^a, Hongzhi Wang^b, Zhanhu Guo^{c,*}

^a School of Environmental and Materials Engineering, Shanghai Second Polytechnic University, Shanghai 201209, China

^b State Key Laboratory for Modification of Chemical Fibers and Polymer Materials, College of Materials Science and Engineering, Donghua University, Shanghai 201620, China

^c Integrated Composites Lab (ICL), Department of Chemical & Biomolecular Engineering, University of Tennessee, Knoxville, TN 37996, USA

ARTICLE INFO

Article history:

Received 12 June 2016

Received in revised form 17 August 2016

Accepted 22 August 2016

Available online 24 August 2016

Keywords:

Electrospinning

Nanocomposites

TiO₂/GO

Photocatalysis

Nanofibers

ABSTRACT

The present study reports the electrospun one-dimensional TiO₂/graphene oxide (GO) composite nanofibers photocatalysts using polyvinylpyrrolidone (PVP) as a fiberizing carrier. Continuous TiO₂ nanofibers segregated by the well-dispersed GO with the content even high as 5 wt% were obtained after the carrier PVP was burnt away at 500 °C. The observed lower excitonic intensity from photoluminescent study in the TiO₂/GO samples than that in bare TiO₂ nanofibers indicated that the recombination of photoinduced electrons and holes in TiO₂ could be effectively inhibited in the composite nanofibers. Photocatalytic studies suggested that the TiO₂/GO composite nanofibers showed higher mobility of charge carriers and enhanced photocatalytic activity than bare TiO₂ nanofibers under visible light irradiation. In addition, photocatalytic performance of the TiO₂/GO composites nanofibers was enhanced with increasing the GO concentration in the composite nanofibers. The results presented herein provide new insights into TiO₂/GO composites materials as high performance photocatalysts with potential uses in environmental remediation.

© 2016 Elsevier B.V. All rights reserved.

1. Introduction

With rising interest in green technology for solving environmental pollution problems, increasing attention has been paid to titanium dioxide (titania, TiO₂) photocatalysts in recent years, as it is cost-effective, has high catalytic stability and is carried out at ambient condition [1]. However, as anatase TiO₂ is a wide bandgap semiconductor, it can only be photoactivated under UV light irradiation (of wavelength shorter than 388 nm), which only accounts for 4% of the solar spectrum [2]. Additionally, the photocatalytic efficiency of TiO₂ could not meet the practical application requirements because of the drawback of poor quantum yield caused by the rapid recombination of photogenerated charge carriers (hole-electron pairs) [3]. Doping TiO₂ with other elements, such as N, C, or Fe was found to broaden the spectral response range to the visible region, but the recombination of electrons and holes may occur on the lattice defects and reduce the subsequent photocatalytic activity [4]. The deposition of noble metals

was reported to produce the Schottky barrier and facilitate electron capture [5]. Therefore, Ag, Ru, and Pt were employed to modify TiO₂ for enhancing UV photocatalytic efficiency and/or visible-light activities [6]. Compared with noble metals, carbon materials are cheaper and easily obtained. In recent years, modifying TiO₂ with a carbonaceous substance on the surface was reported to induce visible-light responsive activity [7]. Various types of carbon, such as graphitic or coke-like carbon or carbonate structural fragments bonding with titanium are proposed as the origin of the visible-light activity [8–10]. As compared with conventional conductive additives, the individual graphene nanosheets, as a new type of one-dimensional (2D) carbon nanomaterial, appear particularly promising to improve the photocatalytic performances owing to its superior electrical conductivity, large specific surface area, and excellent structural flexibility [11]. Even at a very low weight fraction, graphene can serve as an efficient electron conducting network [12]. Consequently, modification of TiO₂ nanomaterials with graphene or graphene oxide has attracted broad interests [13–15]. For example, Anderson et al. synthesized TiO₂-graphene oxide (GO)/thermally reduced graphene oxide (TGO) composites and carried out the photocatalysis in the absence of dissolved oxygen (under nitrogen), and their results confirmed the role of graphene

* Corresponding authors.

E-mail addresses: zhangqh@dhu.edu.cn (Q. Zhang), zguo10@utk.edu (Z. Guo).

as an electron sink and transporter for suppression of electron–hole pair recombination [16]. Cai et al. synthesized visible-light responsive GO/TiO₂ composites with a band gap narrower than 2.43 eV, and they assumed that GO possessed a higher work function than graphene, which made it more possible for electrons to transfer from TiO₂ to GO [17]. Todorova et al. prepared TiO₂/graphene composites photocatalysts, and they found the activity of the TiO₂/RGO composites under visible light in NO_x removal was significantly increased [18]. However, as graphene or GO is not photocatalyst, it only improves the photocatalytic efficiency of TiO₂ during synergy with it. When loading TiO₂ nanoparticles on graphene or GO sheets, the main part is graphene or GO sheets, so the photocatalytic efficiency could not be significantly improved. The nanosized graphene or GO sheets with a high concentration were prone to aggregate in the solution, but the content of TiO₂ may not be enough for the photocatalysis if graphene or GO sheets in a low concentration in the solution.

For photovoltaic and photocatalysis applications, one-dimensional (1D) nanoscaled TiO₂ with modulated morphologies, compositions, and interfaces have obtained considerable attention [19,20]. Especially, compared with photocatalysts in the form of film and nanoparticles, nanofibers are appropriate for practical application because of excellent mobility of charge carriers, high specific surface areas, scattering more light at the red part of the solar spectrum, and the existence of straight pores, which may enhance the adsorption of contaminant molecules [21]. In nowadays, electrospinning has been a facile method to fabricate 1D nanoscaled photocatalysts [22,23]. Lavanya et al. synthesized RGO wrapped tubular and porous rutile TiO₂ nanofibers by electrospinning together with the help of chemical methods for photocatalytic performance in water treatment [24]. Zhu et al. prepared TiO₂–graphene composites to study their photocatalytic properties by electrospinning method; however, probably adding graphene reduced the viscosity of the spinning solution, no continuous nanofibers but rice-shaped TiO₂ composites were obtained [25]. As graphene has a poor dispersion, it is still difficult to fabricate continuous electrospun TiO₂–graphene composite nanofibers with a high graphene content. Compared with graphene, the GO sheets possess lots of functional groups on their surface and thus could be well dispersed in the spinning solution, which help to improve spinnability, and finally obtain continuous nanofibers photocatalysts. However the usage of continuous TiO₂ nanofibers segregated by GO to serve as catalysts for the degradation of methylene blue (MB) and 4-chlorophenol (4-CP) under visible-light irradiation has not been reported.

Herein, we report electrospinning of continuous TiO₂ nanofibers segregated by GO with different contents. The amount of GO in the composite is varied from 0.0 to 5.0 wt% to obtain morphologically stable electrospun nanofibrous mats with increasing photoactivity. The presence of GO in the TiO₂ nanofibers was confirmed using several characterization methods. The recombination of photoinduced electrons and holes in TiO₂ can be effectively inhibited in the composite nanofibers as demonstrated by the photoluminescence spectroscopy and photocurrent tests. The photocatalytic activity of the TiO₂/GO composite nanofibers was investigated on the degradation of methylene blue (MB) and 4-chlorophenol (4-CP) under visible-light irradiation. In addition, the photocatalytic mechanism of the TiO₂/GO composite nanofibers was also discussed in detail.

2. Experimental

2.1. Materials

Graphite powders (30 μm, purity of 99%), tetrabutyl titanate (Ti(OC₄H₉)₄, 97%), acetic acid (glacial, 99.9%), sodium nitrate

(NaNO₃), potassium permanganate (KMnO₄, 98%), sulfuric acid (H₂SO₄, 98%), hydrogen peroxide (H₂O₂, 30%), dimethylformamide (DMF, 99.9%), hydrochloride (HCl, 37%), and 4-CP (C₆H₅ClO, 99%) were all obtained from Sinopharm Chemical Reagent Co., Ltd. The TiO₂ nanoparticles (P25, 20% rutile and 80% anatase, average size of ~20 nm) were purchased from Evonik. Poly(vinyl pyrrolidone) (PVP, M_w ≈ 1.3 × 10⁶) were purchased from Sigma-Aldrich. All the chemicals were used as-received without any further modifications.

2.2. Preparation of GO

The oxidation of graphite powder was achieved according to the modified Hummers' method [26]. Briefly, graphite powder (5 g) and NaNO₃ (2.5 g) were placed in a flask. Concentrated H₂SO₄ (115 mL) was then added slowly with stirring in an ice-water bath. KMnO₄ (15 g) was added gradually over 1 h under stirring and kept stirring for another 2 h. Afterwards, it was stirred at 40 °C for 30 min, then 90 °C for 45 min. Then, dropwise addition of 230 mL distilled water and external heating was introduced to maintain the reaction temperature at 98 °C for 15 min. Finally, the oxidation reaction was terminated by the addition of 700 mL distilled water and 50 mL 30% H₂O₂ solution. The mixture of graphite oxide and oxidants was rinsed with 5% HCl aqueous solution and distilled water to remove the residual metal ions and other impurities. The brown-yellow graphite oxide paste thus obtained was dried at 60 °C under vacuum for 48 h. The required amounts of GO was dispersed in DMF by ultrasonic treatment before mixing with polymer solution. The final solution was concentrated to 4 mg/mL.

2.3. Synthesis of TiO₂/GO nanofibers

The spinning solution for preparing TiO₂ nanofibers contained 4.0 g tetrabutyl titanate, 4.0 mL acetic acid, 1.4 g PVP and 13 mL ethanol. GO solutions were added at different concentrations (0.0–5.0 wt%GO in the obtained TiO₂/GO composites) to the spinning solution. The solution was ultrasonicated for 2 h to ensure the homogeneity. A distance of 10 cm and voltage of 12 kV were maintained between the tip of spinneret and the collector. A grounded wire netting was used as electrode to collect the nanofibers. The as-spun fibers were calcined at 500 °C for 2 h to burn away the organic compounds in air and to obtain inorganic TiO₂/GO nanofibers.

2.4. Sample characterization

The morphologies of the samples were characterized with a field emission scanning electron microscope (FESEM, Hitachi S-4800). TEM images were obtained using a JEM-2100F TEM (JEOL Tokyo Japan) operating at 200 kV. Atomic force microscopy (AFM) images were measured with a NanoScope IV (Veeco, USA) in tapping mode in air. Samples for AFM measurement were prepared by depositing diluted aqueous GO colloidal solution onto freshly cleaved micas and drying at 60 °C under vacuum for 12 h. Thermogravimetric analysis (TG209F1, NETZSCH Instruments Co., Ltd., Bavaria, Germany) was recorded from room temperature to 800 °C at a heating rate of 10 °C min⁻¹ in nitrogen atmosphere. X-ray diffraction (XRD) was carried out on a Rigaku-D/max 2550 PC (Japan) diffractometer with Cu Kα radiation (λ = 1.5406 Å). The samples were characterized with a Fourier transform infrared (FTIR) spectrometer (Nicolet 8700, Bruker Optik GmbH, Ettlingen, Germany) using KBr pellets. DRS spectra were recorded on a PerkinElmer Lambda 950 instrument, using BaSO₄ as the reference sample, in the range of 200–800 nm. Raman spectra were collected on a Fourier transform infrared-Raman spectrometer (NEXUS-5670, Nicolet, USA). X-ray photoelectron spectroscopy (XPS) measurements were performed with a Thermo Scientific K-Alpha using monochromatic Al

K α radiation. Photoluminescence (PL) was measured at room temperature in a PerkinElmer LS55 luminescence spectrometer with a Xenon lamp as the excitation source, and the excited wavelength was 300 nm.

2.5. Photocatalytic activity measurements

In a typical reaction, irradiation was performed with a 500 W xenon lamp and a ZJB 420 filter glass was used to cut off the light with wavelength less than 420 nm. 0.10 g photocatalyst was added into a 450 mL Pexyr photoreactor containing 100 mL 3.8×10^{-5} M MB and 150 mL 1.6×10^{-4} M 4-CP. The concentrations of the solutions were monitored colorimetrically by using a Lambda 35 ultraviolet-visible (UV-vis) absorption spectrophotometer (PerkinElmer, USA) at 655 nm for MB and 224 nm for 4-CP. The absorbance was converted to MB or 4-CP concentration using a standard curve that showed a linear relationship between the concentration and the absorbance at the corresponding wavelength (Fig. S1, Supporting information). The total organic carbon (TOC) of 4-CP was monitored by a TOC Analyzer (Astro TOC UV TURBO,

HACH, USA). The degradation rates and the mineralization degree (%) of 4-CP were calculated using Equation (1) and Equation (2), respectively.

$$\eta(\%) = \frac{C_0 - C}{C_0} \times 100\% \quad (1)$$

$$\phi(\%) = \frac{m_0 - m}{m_0} \times 100\% \quad (2)$$

where C_0 and C are the concentrations of the initial and remaining MB or 4-CP; m_0 and m are the initial and remaining total organic carbon content.

3. Results and discussion

The morphology and microstructure of the as-electrospun composite fibers with different GO contents before calcining at 500 °C is shown in Fig. 1(a–f). It can be observed that all these composite fibers have a one-dimensional texture structure and are randomly oriented forming non-woven mats. The diameter of the bare TiO₂ nanofibers is about 200 nm with the length of individual fibers

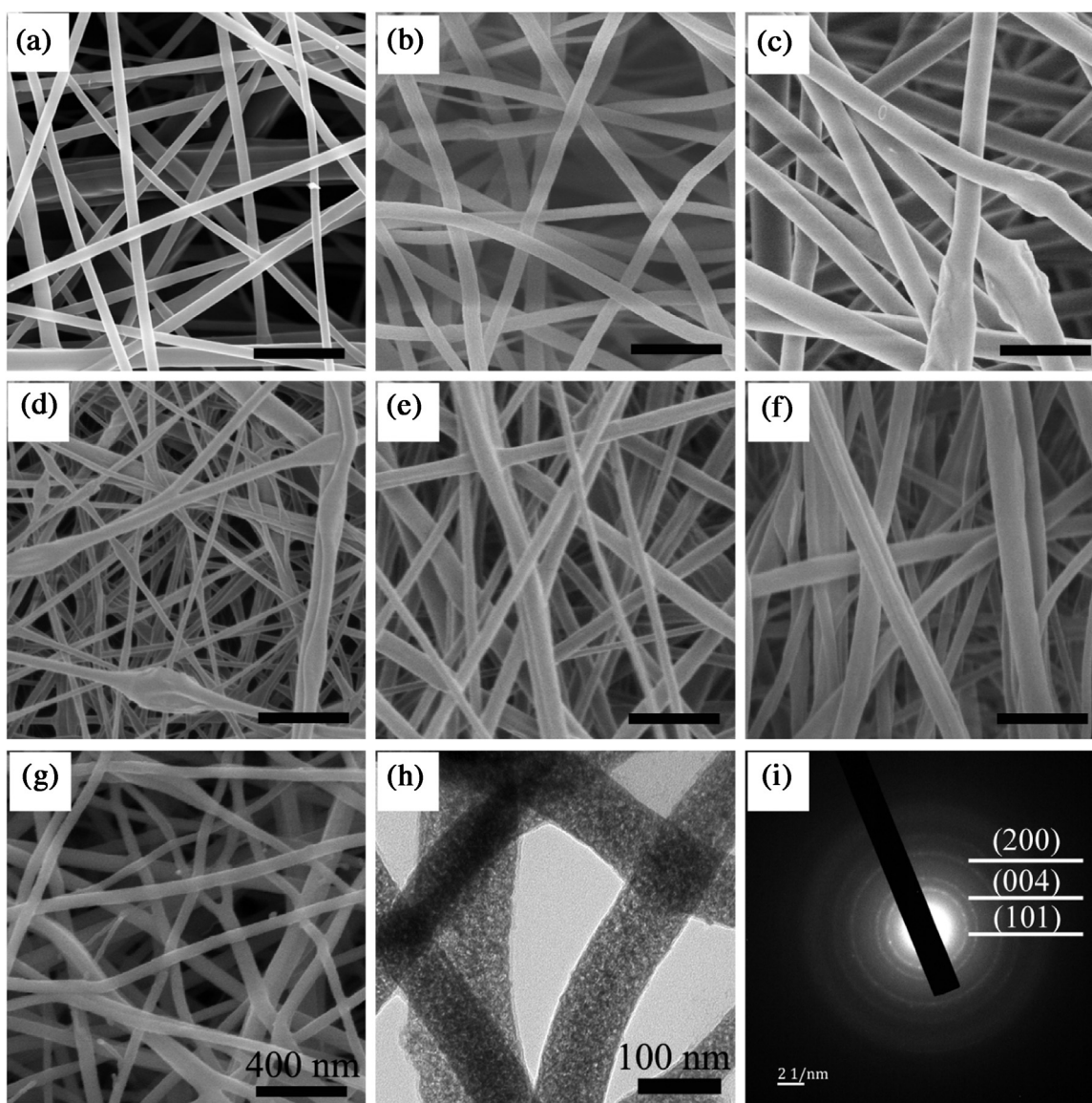


Fig. 1. SEM images of (a) the bare TiO₂ nanofibers, (b) TiO₂/1%GO, (c) TiO₂/2%GO, (d) TiO₂/3%GO, (e) TiO₂/4%GO, and (f) TiO₂/5%GO before calcinations. The inset scale bars are 1000 nm. (g) SEM, (h) TEM images and (i) SAED pattern of the sample TiO₂/3%GO after calcining at 500 °C.

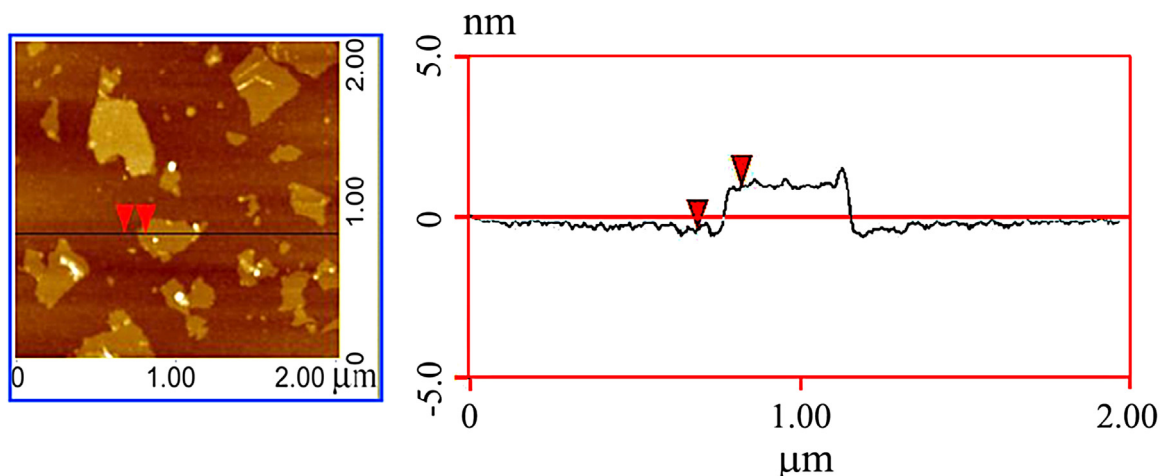


Fig. 2. AFM image and height profile of single-layer GO.

reaching tens of micrometers, Fig. 1a. The diameters of the as-spun nanofibers increased with increasing the GO content in the as-spun nanofibers, Fig. 1b, and c. There were some bubbles exposed on the fibers. The diameters of the as-spun nanofibers decreased in the samples of TiO₂/3%GO and TiO₂/4%GO, as shown in Fig. 1d and e. GO needs to be dispersed in DMF solvent. Increasing the content of GO in the spinning solution, more DMF solvent was needed at the same time, and then the concentrations of PVP and tetrabutyl titanate were reduced. Thus, the diameter of the as-spun nanofibers was decreased after the evaporation of the solvent. The number of bubbles exposed on the fibers was significantly reduced, accompanied with increasing the diameter for the sample TiO₂/5%GO, Fig. 1f. Adding different amounts of GO changed the stability of the spinning solution (such as the concentration, dielectric constant and viscosity). Zhu et al. added graphene in the spinning solution, but it was observed that during the annealing, the continuous fiber morphology was lost, while only rice-shaped TiO₂ composites were obtained [25]. Compared with graphene, it was reported that GO with lots of organic group on their surface could be well dispersed in several organic solutions such as DMF [27]. In addition, some minor adjustments of the spinning parameters were needed to make the electrospinning process smoothly carried out, which may make the morphology of the as-spun nanofibers correspondingly changed. After calcined at 500 °C, the continuous fibrous morphology still exists, but the average diameter of the nanofibers changed to ~100 nm, and the bubbles were disappeared as shown in the SEM and TEM images of the sample TiO₂/3%GO (Fig. 1g and h). The GO was not identified by the SEM or TEM, possibly attributed to that GO were integrally connected to the inorganic nanoparticles within the nanofibers. The selected area electron diffraction (SAED) pattern is consistent with the tetragonal structure of anatase TiO₂, with strong ring patterns being assigned to (1 0 1), (0 0 4), and (2 0 0) planes of anatase (Fig. 1i) [28]. Fig. 2 shows an AFM image of GO sheets deposited on freshly cleaved mica from aqueous suspension. According to the statistical evaluation, the mean thickness of a single GO sheet was ~1.0 nm. The 1.0 nm thickness and 0.5 μm length of the sheet in Fig. 2 indicate that the GO sheets exist in single layers and disperse thoroughly in the DMF solution. It has been reported that graphene fibers could be fabricated by wet-spinning of a concentrated GO liquid crystal solution [29]. However, the mechanism for fabricating graphene fibers by wet-spinning methodology was different from fabricating nanofibers by electrospinning method. The spinning solution requires a higher viscosity for fiberizing GO during the electrospinning process. As a result, some polymer materials (such as polyvinyl alcohol, polyvinylpyrrolidone and so on) need to be added as fiber-

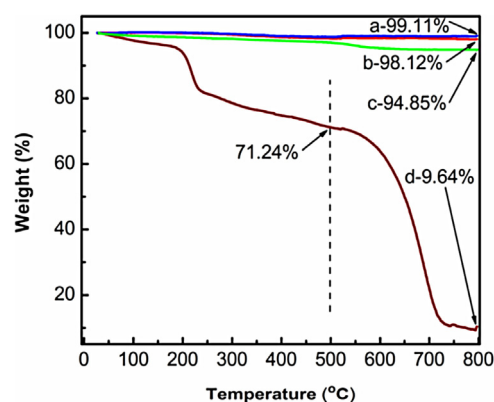


Fig. 3. TGA curves of the samples of (a) the bare TiO₂ nanofibers, (b) TiO₂/1%GO, (c) TiO₂/5%GO, and (d) pure GO sheets.

izing carrier. As the removal of fiberizing carrier may damage the nanofiber structure, there was no literature reported about fabricating graphene or GO nanofibers via electrospinning method from GO solution without adding fiberizing carrier up to now.

Fig. 3 shows the TGA curves of the samples of bare TiO₂ nanofibers (curve a), TiO₂/1%GO (curve b), TiO₂/5%GO (curve c) calcined at 500 °C and pure GO (curve d). As shown in Fig. 3, the bare TiO₂ nanofibers have a low weight loss of 0.89% due to water evaporation and combustion of carbon residue. It also indicates that almost all PVP was burnt away in the nanofibers. The sample TiO₂/1%GO and TiO₂/5%GO have a low weight loss of 1.88% and 5.15% respectively. Subtracted the parts of water evaporation and combustion of carbon residue in PVP, the GO contents in TiO₂/1%GO and TiO₂/5%GO were calculated to be 0.99% and 4.26%. The TGA curves of pure GO can be distinctly divided into three stages. The first stage is 30–180 °C with the weight loss about 4.5%, indicating the loss of solvent such as water and ethanol in GO [30]. At the second stage (180–550 °C), the weight loss of the GO was about 33%, which might be ascribed to the degradation of GO [31]. The weight loss of pure GO at 500 °C was 28.76%, indicating that after calcining at 500 °C there may be some distortion on GO, but the main part of GO still exists in the nanofibers. At the last stage (550–800 °C), the weight loss of pure GO was about 90.36%, which was possibly caused by the combustion of GO sheets.

Fig. 4A shows the XRD patterns of the nanofibers with different GO contents after calcinations at 500 °C. The diffraction peaks of the nanofibers can be indexed to (1 0 1), (0 0 4), (2 0 0), (1 0 5), (2 1 1), (2 0 4) and (2 1 5) crystal planes of TiO₂ (JCPDS File No.

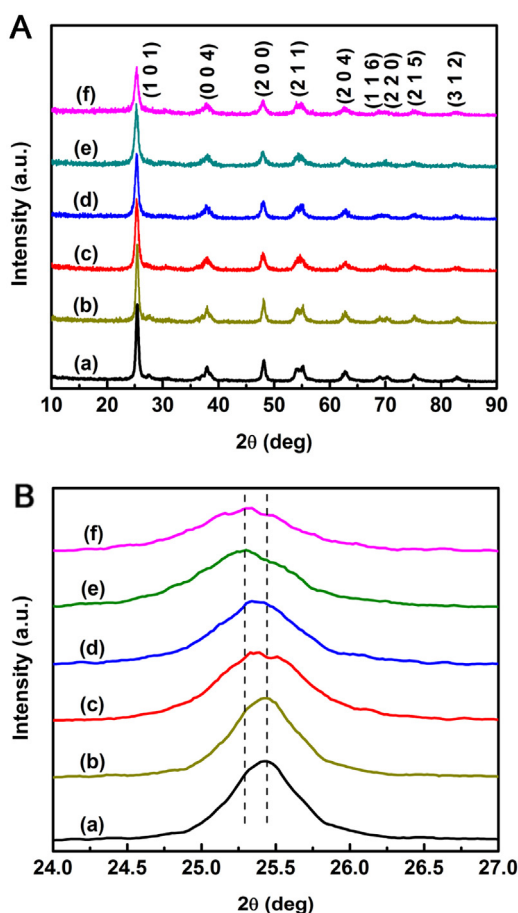


Fig. 4. XRD patterns of (a) bare TiO₂ nanofibers, (b) TiO₂/1%GO, (c) TiO₂/2%GO, (d) TiO₂/3%GO, (e) TiO₂/4%GO, and (f) TiO₂/5%GO after calcinations with 2θ in (A) 10°–90° and (B) 24.0°–27.0°.

21–1272) [32]. All the peaks of the nanofibers can be assigned to the anatase phase. The crystallite sizes are 15.6, 13.3, 13.2, 12.9, 12.8 and 12.6 nm for bare TiO₂ nanofibers, TiO₂/1%GO, TiO₂/2%GO, TiO₂/3%GO, TiO₂/4%GO, and TiO₂/5%GO after calcinations, respectively, calculated from X-ray line broadening (ω) according to the Scherrer formula:

$$d = 0.89\lambda / \omega \cos \theta \quad (3)$$

where λ is the X-ray wavelength, 1.5406 Å (Cu K α), and θ is the diffraction angle. The intensity of diffraction peaks decreased with increasing the GO content in the composites, also suggesting that finer crystallite size of TiO₂ was formed in the presence of the nanofibers. Additionally, the most intense diffraction peaks of (1 0 1) plane of the nanofibers are displaced to lower 2 θ values gradually with increasing the GO content in the composites (Fig. 4B). It can be attributed to adding GO into the TiO₂ nanofibers that inhibited the growth of the TiO₂ crystallites.

Fig. 5 shows the FTIR spectra of the bare TiO₂ nanofibers, TiO₂/4%GO, and pure GO. All the three samples exhibit very strong peaks between 3400 and 3450 cm⁻¹ corresponding to the adsorbed water or O–H stretching vibration of hydroxyl groups [16]. The peak at 1638 cm⁻¹ represents the O–H distorting vibration is due to water molecules [33]. The peaks at 1385 and 500–700 cm⁻¹ in the bare TiO₂ nanofibers originate from the Ti–O and Ti–O–Ti stretching mode, respectively [23,33]. For the pure GO sheets, several characteristic peaks such as those at 1729 (C=O carboxyl or carbonyl stretching vibration), 1392 (O–H deformations in the C–OH groups), 1228 (C–OH stretching vibration) and 1050 cm⁻¹ (C–O stretching vibrations in the epoxy group) were observed [16]. The

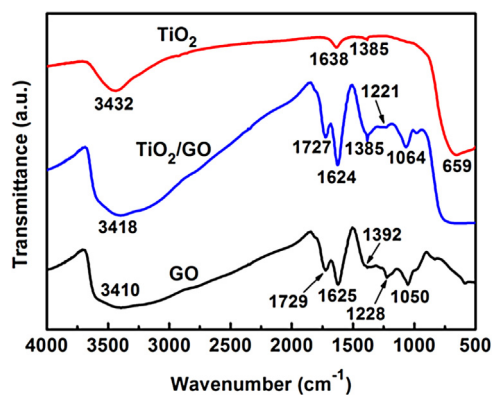


Fig. 5. FTIR spectra of the bare TiO₂ nanofibers, the sample TiO₂/4%GO and pure GO.

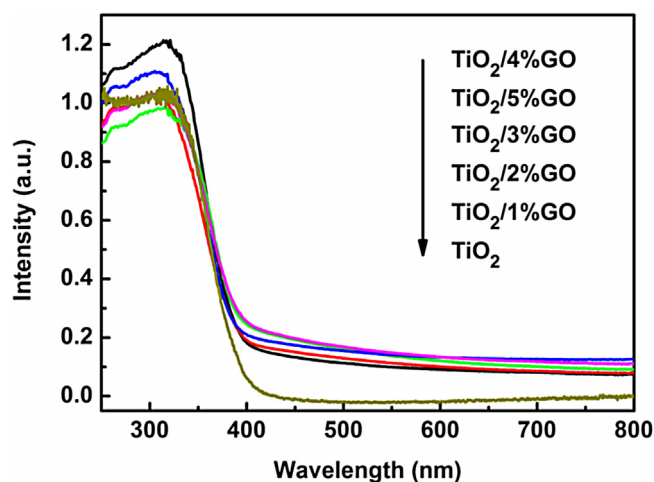


Fig. 6. UV-vis DRS spectra of different samples.

peak at around 1625 cm⁻¹ may be attributed to the deformation mode of the adsorbed water and non-oxidised graphitic domains. The FTIR spectrum of TiO₂/GO nanofibers exhibits the absorption peaks at almost the same positions as pure GO, indicating that the calcination of the as-spun fibers at 500 °C in air did not reduce GO in the TiO₂/GO composite nanofibers. The presence of peaks at 1727, 1385, 1221 and 1064 cm⁻¹ indicates the existence of functional groups of carboxyl, hydroxyl and epoxy groups in the TiO₂/GO composite nanofibers. The C=O stretching of the –COOH groups of GO sheets observed at 1727 cm⁻¹ can help to interpret the connection between the graphene sheets and TiO₂ [34]. The –OH, –COOH, and –C–O–C groups on the surface of GO sheets and –OH groups on TiO₂ allow GO contact with TiO₂ closely in the molecular level [33,35].

The UV-vis DRS spectra of the bare TiO₂ nanofibers and the TiO₂/GO nanofibers with different GO contents are shown in Fig. 6. The main absorption edge for bare TiO₂ nanofibers is estimated to be 402 nm, which can be attributed to the intrinsic absorption band derived from the band gap transition from O 2p to Ti 3d orbital [36]. The band gap energy was calculated to be 3.1 eV using the relation $E_g = 1240/\lambda$, where λ is the onset absorption wavelength (402 nm) [37]. The absorption edge of the TiO₂/GO nanofibers is also at 402 nm, implying that GO is not incorporated into the lattice of TiO₂. The TiO₂/GO nanofibers have an enhanced response in the whole visible-light region due to the interaction between TiO₂ and GO through the O=C=O bond originated from the –COOH groups connecting the graphene and TiO₂, which is proposed as the origin of the visible light activity [34,38]. The UV-vis DRS spectra of the TiO₂/GO nanofibers are different from those of the TiO₂/carbon

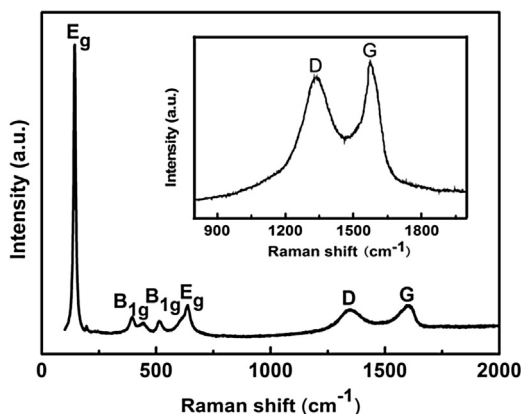


Fig. 7. Raman spectra of the sample $\text{TiO}_2/4\%\text{GO}$ and pure GO (inset).

structured materials; the absorption edge of TiO_2 is largely covered by carbon that has a strong absorbance in the visible-light region [39]. With increasing the GO content in the TiO_2 nanofibers, the intensity of the visible-light absorbance was also increased in the visible light range of 400–700 nm. However, the intensity changes between TiO_2/GO nanofibers samples were not as evident as the intensity changes from bare TiO_2 to TiO_2/GO nanofibers samples. This indicates that coupling with GO could extend the optical absorption of TiO_2 into the visible-light region. The white TiO_2 nanofibers changed into dark gray after incorporating GO sheets into the nanofibers.

Fig. 7 shows the Raman spectra of the sample $\text{TiO}_2/4\%\text{GO}$ and pure GO (inset). The sample $\text{TiO}_2/4\%\text{GO}$ exhibits four major Raman bands at 156, 379, 518, and 635 cm^{-1} in the range of 0–1000 cm^{-1} , which can be attributed to the Raman-active modes of anatase phase with the symmetries of E_g , B_{1g} , A_{1g} and E_g , respectively [40]. In addition, two prominent peaks at 1350 and 1580 cm^{-1} , named the D and G band, were also observed, indicating the successful incorporation of GO into the composite nanofibers [41]. The D band is the symmetric A_{1g} mode and has been ascribed to the edges, defects, dangling bonds and disordered carbon, while the G band is the E_{2g} mode and corresponds to ordered sp^2 -bonded carbon atoms [42]. Therefore the intensity ratio of the D to G band (I_D/I_G) is a measure of the disorder, as expressed by the sp^2/sp^3 carbon ratio, which is a critical characteristic referring to the electrical conductivity [43]. The I_D/I_G values of the pure GO and the sample $\text{TiO}_2/4\%\text{GO}$ were calculated to be 0.90 and 0.94, indicating that after calcination the defects in the sample $\text{TiO}_2/4\%\text{GO}$ were slightly increased due to a larger quantity of edges caused by the distortion of GO sheets in the TiO_2 nanofibers.

To investigate the chemical nature of the resultant nanofibers, X-ray photoelectron spectroscopy (XPS) was performed on both GO sheets and TiO_2/GO nanofibers, which provided an exact elemental composition in the top 1–12 nm of the sample surface. The XPS survey (Fig. 8a) confirms the C, O and Ti composition of the TiO_2/GO nanofibers, while there were only C and O peaks detected in the GO sample. The high resolution C 1s XPS spectra of GO and TiO_2/GO nanofibers (Fig. 8b) include three components: nonoxygen ring C (284.1 eV, containing C–C, C=C, and C–H bonds), C–O (286.6 eV), and O–C=O (288.5 eV) [23], which are consistent with the FTIR spectra. The peak area ratios of the C–O and O–C=O bonds to the C–C bonds were respectively expressed as $A_{\text{C-O}}/A_{\text{C-C}}$ and $A_{\text{O-C=O}}/A_{\text{C-C}}$ and estimated for comparison. The values of $A_{\text{C-O}}/A_{\text{C-C}}$ and $A_{\text{O-C=O}}/A_{\text{C-C}}$ were 0.74 and 0.28 for bare GO, and 0.18 and 0.11 for the TiO_2/GO nanofibers. This means that more than one half of the oxygen-containing groups were removed for GO, after being inserted into TiO_2 nanofibers and calcined at 500°C . No peak in the C 1s or the Ti 2p spectra can be assigned to Ti–C bond-

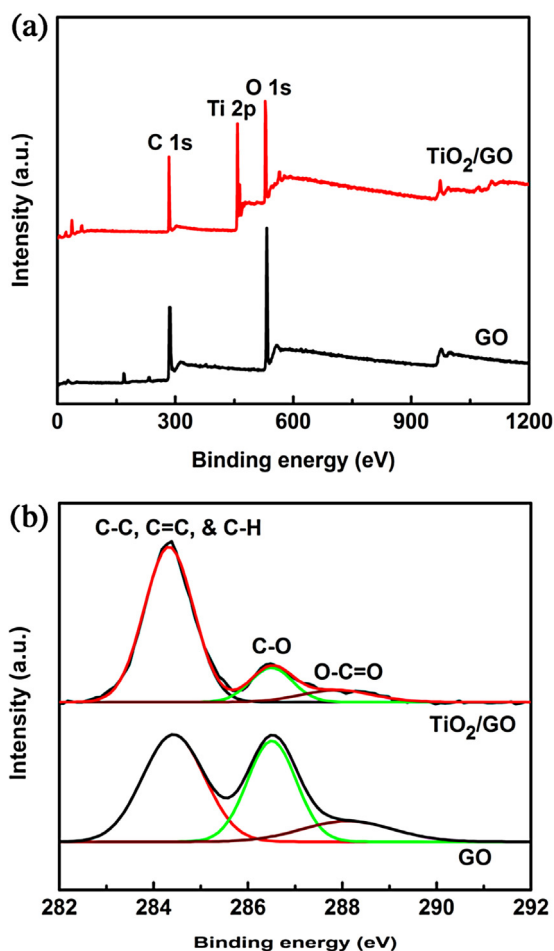


Fig. 8. (a) XPS survey and (b) high resolution C 1s XPS spectra of TiO_2/GO nanofibers and GO nanosheets.

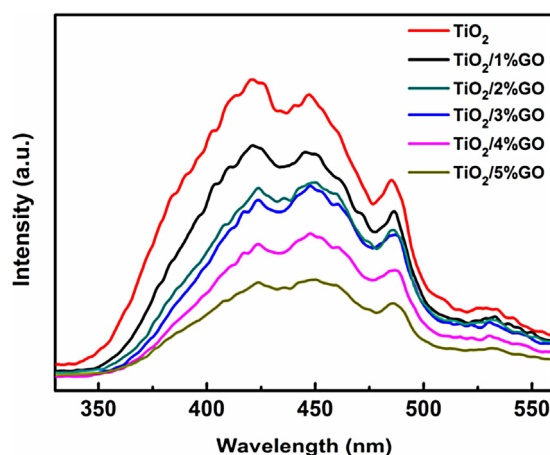


Fig. 9. PL spectra of different samples.

ing, which has a binding energy of ~ 282 and ~ 455 eV, respectively [44,45]. Hence, no Ti–C covalent bonding was formed between the TiO_2 fibers and the GO sheets. As observed in the FTIR spectra, the O–C=O (288.5 eV) peak is originated from the –COOH groups of GO sheets in the TiO_2/GO composite nanofibers that helps to connect the graphene sheets and TiO_2 surfaces [34].

The PL analysis has been performed to investigate the efficiency of charge carrier trapping and transfer behavior of the photoinduced electrons and holes [46]. Fig. 9 represents the PL spectra

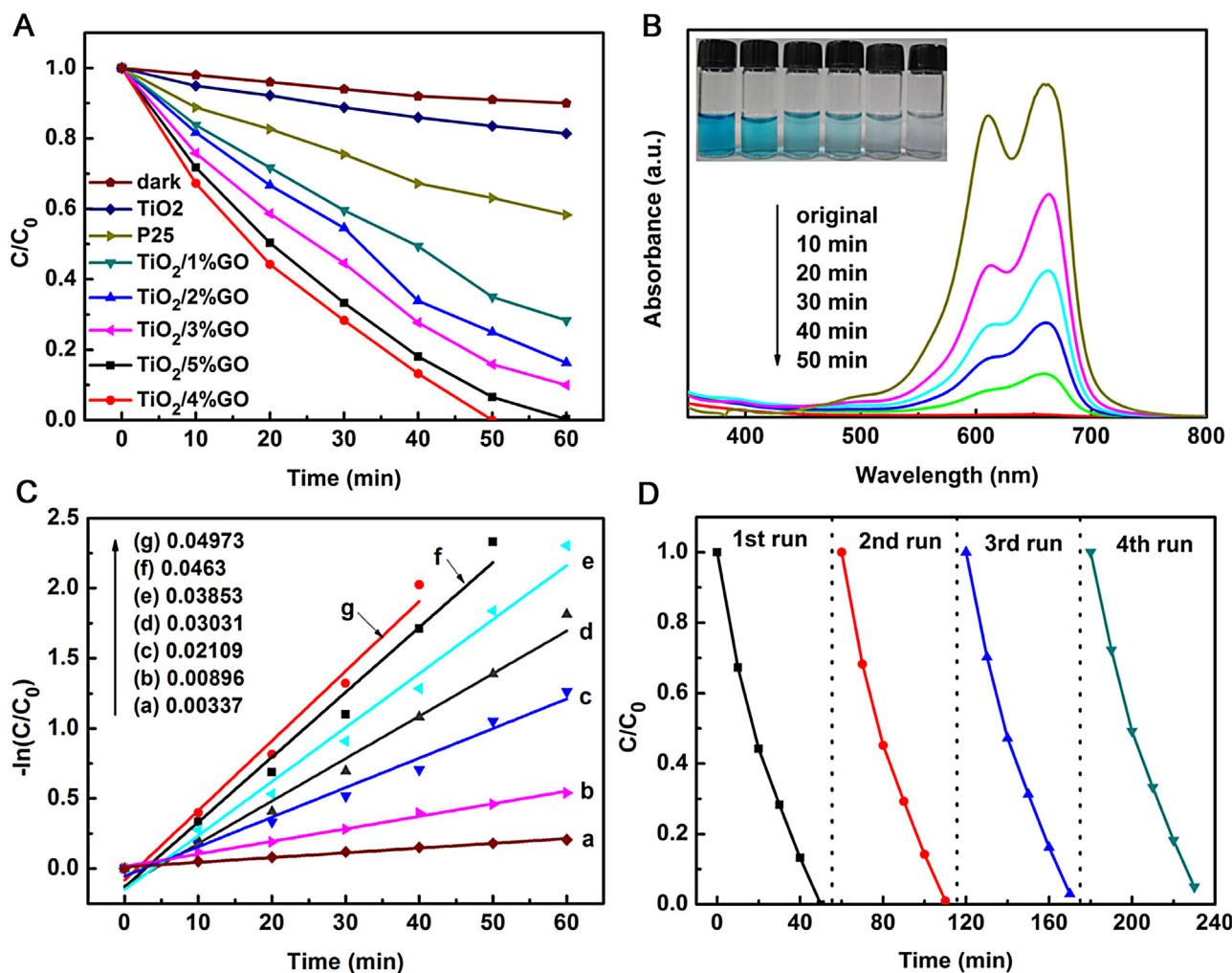


Fig. 10. (A) The photocatalytic degradation of MB over different samples. (B) The absorption spectra of MB photodegraded by TiO₂/4%GO after different time. (C) Kinetic linear simulation curves of photocatalytic degradation MB over different samples: (a) bare TiO₂ nanofibers, (b) P25, (c) TiO₂/1%GO, (d) TiO₂/2%GO, (e) TiO₂/3%GO, (f) TiO₂/5%GO and (g) TiO₂/4%GO. (D) Recyclability of the photocatalytic decomposition of MB for TiO₂/4%GO.

of the bare and GO added TiO₂ nanofibers. All the samples exhibited obvious PL signals under irradiation with 300 nm light. The PL intensity decreased with increasing the GO content in the TiO₂ nanofibers. The weakened PL signal is attributed to the migration of photoelectrons from the TiO₂ surfaces to GO sheet, resulting in a decrease in the radiation recombination of photoinduced electrons on the TiO₂ surfaces [47]. When GO formed a p-type semiconductor, a p/n heterojunction could be clearly observed [17]. The potential difference between TiO₂ and GO allowed photoelectrons to easily migrate from the TiO₂ surfaces to the GO conduction band. This resulted in a decrease in the recombination of photoinduced electrons on the TiO₂ surfaces and a further weakened PL signals. The efficient charge separation could increase the lifetime of the charge carriers and enhance the efficiency of the interfacial charge transfer to the surface, and then account for a higher activity of TiO₂/GO nanofibers.

The photocatalytic degradation of MB has been chosen as a model reaction to evaluate the photocatalytic activities of the TiO₂/GO nanofibers. For comparison, the photocatalytic degradation of MB by bare TiO₂ nanofibers, Evonik P25 and TiO₂/GO nanofibers in the dark was also carried out under the same condition. Fig. 10A shows the degradation curves of MB with different samples. The TiO₂/GO nanofibers in the dark exhibited little photolysis. The TiO₂/GO composite nanofibers exhibited higher photocatalytic activity than Evonik P25 and bare TiO₂

nanofibers. Generally, with increasing the GO content, the composite TiO₂/GO nanofibers exhibited higher photocatalytic activity. The diameters of bare TiO₂ and GO sheets are much less than the carrier diffusion length of 60–100 μm [48], while the electrons and holes can be efficiently separated in the TiO₂/GO composite nanofibers. Notably, the time for an entire decolorization of MB over TiO₂/4%GO and TiO₂/5%GO was about 50 min and 60 min. The photocatalytic efficiency of TiO₂/5%GO was lower than that of TiO₂/4%GO, meaning that further increasing the GO content in the nanofibers may reduce the photogenerated carriers induced by TiO₂. The photocatalytic rates for MB under UV irradiation are shown in Fig. S2 in the Supporting information, suggesting the function of heterojunction in leading to the efficient charge separation and the resulting high photocatalytic activity. Fig. 10B shows the changes in the UV-vis absorption spectra of the MB solution with TiO₂/4%GO as the photocatalyst. The decomposition rate of MB was very fast at the beginning and then slowed. The sharp decrease indicates that TiO₂/4%GO provided excellent removal of MB. The digital photo shows that, after 50 min, the color of MB was entirely decolorized over TiO₂/4%GO (Fig. 10B, inset). In order to better understand the photocatalytic efficiency of the above photocatalysis, the photocatalytic degradation kinetics of MB was also investigated. The photocatalytic degradation process is fit to pseudo-first-order kinetics [49], $-\ln(C/C_0) = kt$, where k is the photocatalytic reaction apparent rate constant and t is

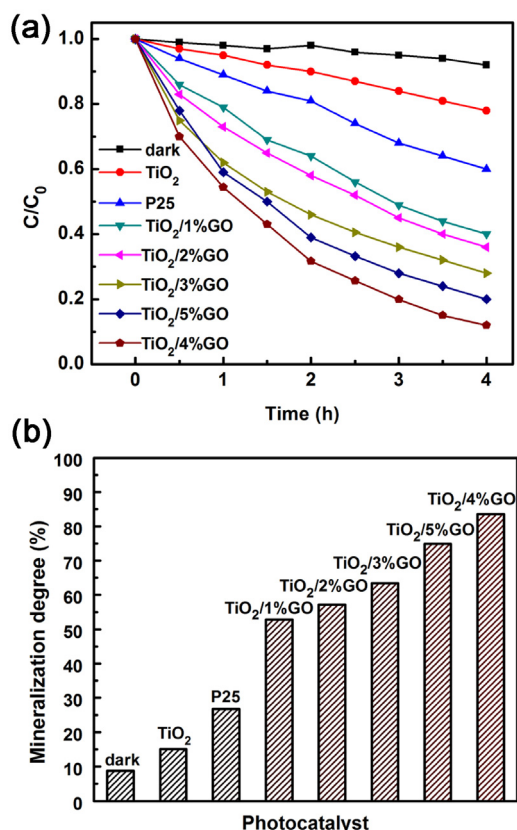


Fig. 11. (a) The degradation rates and (b) mineralization degrees (%) of 4-chlorophenol photocatalyzed over different samples.

the light irradiation time, due to the low initial concentrations of the reactants (~ 12 mg/L). Fig. 10C shows the effect of different samples on the kinetics of MB under visible light irradiation. The calculated value of apparent rate constant k from the corresponding slope of the pseudo-first-order linear simulation curve is shown in the inset of Fig. 10C. It is seen that the k values for $TiO_2/4\%GO$, $TiO_2/5\%GO$, $TiO_2/3\%GO$, $TiO_2/2\%GO$, $TiO_2/1\%GO$, P25 and bare TiO_2 nanofibers are 0.04973, 0.0463, 0.03853, 0.03031, 0.02109, 0.00896 and 0.00337 min^{-1} , respectively. Obviously, the k value of the $TiO_2/4\%GO$ is far higher than those of the others,

and is 5.6 and 14.8 times higher than those of P25 and bare TiO_2 nanofibers, respectively, suggesting that the introduction of GO could extend the light absorption spectrum of TiO_2 and thus highly improve the visible light photocatalytic performance. The photocatalytic efficiency under visible light irradiation estimated by the k value follows the order: $TiO_2/4\%GO > TiO_2/5\%GO > TiO_2/3\%GO > TiO_2/2\%GO > TiO_2/1\%GO > P25 >$ the bare TiO_2 nanofibers. Furthermore, the TiO_2/GO composite nanofibers photocatalyst can be effectively recycled at least four times without an apparent decrease in its photocatalytic activity, which demonstrates its high stability (Fig. 10D).

Though the photocatalytic degradation of MB in water by TiO_2/GO composite nanofibers is efficient, MB can work as a photosensitizer to inject electrons to conduction band (CB) of metal oxide particles, undergoing self-oxidative degradation [50,51]. The MB solution was tested without photocatalysts under the same experimental conditions; the C/C_0 value was 0.85 after 60 min. It indicates that the sensitization mechanism indeed accelerated the degradation of MB molecule in the solution. However, comparing with photocatalysis, the self-oxidative degradation caused by sensitization mechanism was not remarkable. The degradation rates of 4-CP were also studied photocatalyzed over TiO_2/GO composite nanofibers. The 4-CP solution without photocatalysts exhibited little photolysis under visible-light illumination, with the C/C_0 value of 0.96, implying that 4-CP was stable without self-oxidative degradation. The photocatalytic degradation of 4-CP over different samples was shown in Fig. 11. The C/C_0 values were 0.77 and 0.59 for the bare TiO_2 nanofibers and P25 respectively. The photocatalytic reaction time reached more than 4 h, as the carbon chains on the benzene ring were much sturdier than MB molecule. Notably, all the C/C_0 values were lower than 0.40 for the TiO_2/GO composite nanofibers, especially the C/C_0 values were 0.19 and 0.12 for two of the most efficient catalysts of $TiO_2/5\%GO$ and $TiO_2/4\%GO$. The mineralization degree (%) of more than 80% (calculated from the ratio between TOC final values and initial TOC content in the tests) indicated that more than 80% 4-CP was mineralized with $TiO_2/4\%GO$ under visible-light illumination.

The heterostructure which facilitates the charge transfer may account for the enhancement of the photocatalytic activity of TiO_2/GO nanofibers. Fig. 12 shows the schematic diagram of the internal micron structure and electron-hole pair separation in the TiO_2/GO nanofibers. As shown in Fig. 12, the electrospun TiO_2 nanofibers segregated by GO and formed heterojunction with the photogenerated carrier diffusion between them. When the TiO_2/GO

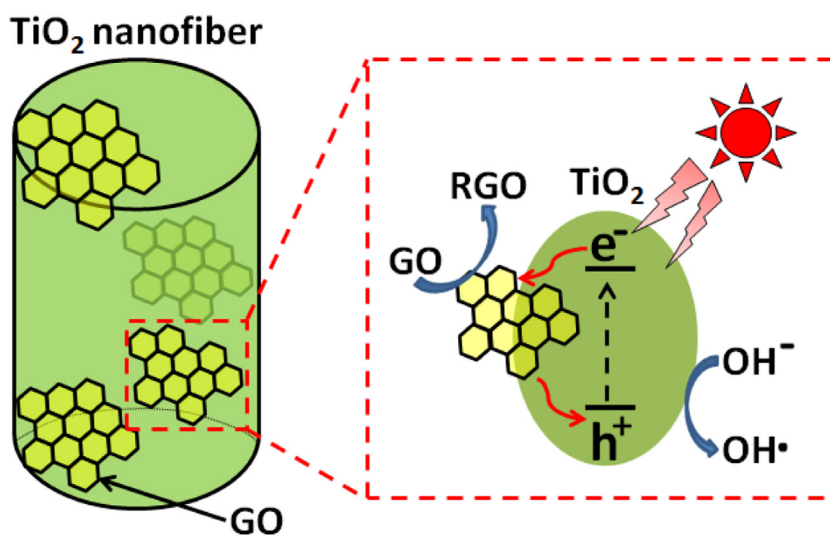


Fig. 12. Schematic diagram showing the internal structure and electron-hole pair separation in the TiO_2/GO nanofibers.

heterojunction is excited with photon energy higher than or equal to the band gap of TiO₂/GO, the electrons in the valence band (VB) could be excited to the CB with simultaneous generation of the same amount of holes in the VB. The photogenerated electrons transfer occurred from the CB of TiO₂ to GO. The accumulated electrons serve to interact with the GO sheets in order to reduce certain functional groups on the surface of GO (RGO) [52]. Holes were then captured by surface hydroxyl groups (OH⁻) on the photocatalyst surface to yield hydroxyl radicals (OH[•]) [53]. The OH[•], as strong oxidizing agents, degraded the organic molecules of MB and 4-CP [54]. This further promotes the photogenerated electrons to interact with the GO sheets. The efficient charge separation increases the lifetime of the charge carriers and enhances the efficiency of the interfacial charge transfer to surface of the photocatalyst, and then, accounts for a higher photocatalytic activity of the TiO₂/GO photocatalysts.

4. Conclusions

The present study reports the preparation of well-defined and structurally stable TiO₂ nanofibers segregated by GO with different contents using electrospinning technology. The presence of GO in the TiO₂ nanofibers was confirmed using several characterization methods. These TiO₂/GO composite nanofibers demonstrated enhanced visible-light absorption and increased photocatalytic degradation of organic pollutants. The investigation of photocatalytic ability indicated that TiO₂/GO composite nanofibers possessed higher photocatalytic activity than Evonik P25 and the bare TiO₂ nanofibers for the degradation of MB and 4-CP molecules under visible-light irradiation due to the enhanced separation efficiency of photogenerated electron-hole pairs. It is expected that such nanofibers photocatalysts would provide great impetus to the practical application in environmental remediations.

Acknowledgements

The project was funded by State Key Laboratory for Modification of Chemical Fibers and Polymer Materials, Donghua University (No. LK1518), School Funds of Shanghai Second Polytechnic University (No. EGD15XQD05), Young College Teachers' Training Scheme of Shanghai (No. ZZZZEGD15013), Natural Science Foundation of Shanghai (Nos. 16ZR1412600, 15ZR1416900), Natural Science Foundation of China (Nos. 51572046, 51503035), the Science and Technology Commission of Shanghai (No. 13JC1400200), the Program for Professor of Special Appointment (Eastern Scholar) at Shanghai Institutions of Higher Learning, the Program of Introducing Talents of Discipline to Universities (No. 111-2-04), and Shanghai Eastern Scholarship program.

Appendix A. Supplementary data

Supplementary data associated with this article can be found, in the online version, at <http://dx.doi.org/10.1016/j.apcatb.2016.08.056>.

References

- [1] J.H. Mo, Y.P. Zhang, Q.J. Xu, J.J. Lamson, R.Y. Zhao, *Atmos. Environ.* 43 (2009) 2229–2246.
- [2] M.R. Hoffmann, S.T. Martin, W.Y. Choi, D.W. Bahnemann, *Chem. Rev.* 95 (1995) 69–96.
- [3] H.H. Gan, G.K. Zhang, Y.D. Guo, *J. Colloid Interf. Sci.* 386 (2012) 373–380.
- [4] B.C. Qiu, C.C. Zhong, M.Y. Xing, J.L. Zhang, *RSC Adv.* 5 (2015) 17802–17808.
- [5] A.L. Linsebigler, G. Lu, J.T. Yates Jr., *Chem. Rev.* 95 (1995) 735–758.
- [6] H. Tong, S.X. Ouyang, Y.P. Bi, N. Umezawa, M. Oshikiri, J.H. Ye, *Adv. Mater.* 24 (2012) 229–251.
- [7] C. Chen, M. Long, H. Zeng, W. Cai, B. Zhou, J. Zhang, Y. Wu, D. Ding, D. Wu, *J. Mol. Catal. A* 314 (2009) 35–41.
- [8] C. Lettmann, K. Hildenbrand, H. Kisch, W. Macyk, W.F. Maier, *Appl. Catal. B: Environ.* 32 (2001) 215–227.
- [9] L.W. Zhang, H.B. Fu, Y.F. Zhu, *Adv. Funct. Mater.* 18 (2008) 2180–2189.
- [10] P. Zabeck, J. Eberl, H. Kisch, *Photochem. Photobiol. Sci.* 8 (2009) 264–269.
- [11] P.V. Kamat, *J. Phys. Chem. Lett.* 2 (2011) 242–251.
- [12] M. Liang, L. Zhi, *J. Mater. Chem.* 19 (2009) 5871–5878.
- [13] S.D. Perera, R.G. Mariano, K. Vu, N. Nour, O. Seitz, Y. Chabal, K.J. Balkus, *ACS Catal.* 2 (2012) 949–956.
- [14] D. Maruthamani, D. Divakar, M. Kumaravel, *J. Ind. Eng. Chem.* 30 (2015) 33–43.
- [15] P. Fernandez-Ibanez, M.I.P. olo-Lopez, S. Malato, S. Wadhwa, J.W.J. Hamilton, P.S.M. Dunlop, R. D'sa, E. Magee, K. O'shea, D.D. Dionysiou, *Chem. Eng. J.* 261 (2015) 36–44.
- [16] H. Adamu, P. Dubey, J.A. Anderson, *Chem. Eng. J.* 284 (2016) 380–388.
- [17] C. Chen, W.M. Cai, M.C. Long, B.X. Zhou, Y.H. Wu, D.Y. Wu, Y.J. Feng, *ACS Nano* 4 (2010) 6425–6432.
- [18] A. Trapalis, N. Todorova, T. Giannakopoulou, N. Boukos, T. Speliotis, D. Dimotikali, J.G. Yu, *Appl. Catal. B: Environ.* 180 (2016) 637–647.
- [19] K. Dick, K. Deppert, M.W. Larsson, T. Martensson, W. Seifert, L.R. Wallenberg, L. Samuelson, *Nat. Mater.* 3 (2004) 380–384.
- [20] W.I. Park, G.C. Yi, M. Kim, S.J. Pennycook, *Adv. Mater.* 15 (2003) 526–529.
- [21] X. Feng, K. Shankar, O.K. Varghese, M. Paulose, T.J. Latempa, C.A. Grimes, *Nano Lett.* 8 (2008) 3781–3786.
- [22] H.L. Qu, S.Y. Wei, Z.H. Guo, *J. Mater. Chem. A* 1 (2013) 11513–11528.
- [23] Y.Q. Dai, Y. Jing, J. Zeng, Q. Qi, C.L. Wang, D. Goldfeld, C.H. Xu, Y.P. Zheng, Y.M. Sun, *J. Mater. Chem.* 21 (2011) 18174–18179.
- [24] T. Lavanya, M. Dutta, K. Satheesh, *Sep. Purif. Technol.* 168 (2016) 284–293.
- [25] P.N. Zhu, N.A. Sreekumaran, S.J. Peng, S.Y. Yang, R. Seeram, *ACS Appl. Mater. Interfaces* 4 (2012) 581–585.
- [26] Z. Liu, J.T. Robinson, X. Sun, H. Dai, *J. Am. Chem. Soc.* 130 (2008) 10876–10877.
- [27] J.L. Paredes, S. Villar-Rodil, A. Martínez-Alonso, J.M.D. Tascón, *Langmuir* 24 (2008) 10560–10564.
- [28] L. Zhang, Y.G. Li, Q.H. Zhang, G.Y. Shi, H.Z. Wang, *Chem. Lett.* 40 (2011) 1371–1373.
- [29] Z. Xu, H.Y. Sun, X.L. Zhao, C. Gao, *Adv. Mater.* 25 (2013) 188–193.
- [30] G.L. Shao, Y.G. Lu, F.F. Wu, C.L. Yang, F.L. Zeng, Q.L. Wu, *J. Mater. Sci.* 47 (2012) 4400–4409.
- [31] X.G. Mei, J.Y. Ouyang, *Carbon* 49 (2011) 5389–5397.
- [32] L. Zhang, Y.G. Li, Q.H. Zhang, H.Z. Wang, *CrystEngComm* 15 (2013) 5986–5993.
- [33] S. Umrao, S. Abraham, F. Theil, S. Pandey, V. Ciobotă, P.K. Shukla, C.J. Rupp, S. Chakraborty, R. Ahuja, J. Popp, B. Dietzek, A. Srivastava, *RSC Adv.* 4 (2014) 59890–59901.
- [34] J.J. Fan, S.W. Liu, J.G. Yu, *J. Mater. Chem.* 22 (2012) 17027–17036.
- [35] Y.L. Min, K. Zhang, W. Zhao, F.C. Zheng, Y.C. Chen, Y.G. Zhang, *Chem. Eng. J.* 193–194 (2012) 203–210.
- [36] J.K. Burdett, T. Hughbanks, G.J. Miller, J.W. Richardson, J.V. Smith, *J. Am. Chem. Soc.* 109 (1987) 3639–3646.
- [37] C.F. Lin, C.H. Wu, Z.N. Onn, *J. Hazard. Mater.* 154 (2008) 1033–1039.
- [38] L.W. Zhang, H.B. Fu, Y.F. Zhu, *Adv. Funct. Mater.* 18 (2008) 2180–2189.
- [39] L. Zhao, X.F. Chen, X.C. Wang, Y.J. Zhang, W. Wei, Y.H. Sun, M. Antonietti, M. Titirici, *Adv. Mater.* 22 (2010) 3317–3321.
- [40] T. Ohsaka, F. Izumi, Y. Fujiki, *J. Raman Spectrosc.* 7 (1978) 321–324.
- [41] K.N. Kudin, B. Ozbas, H.C. Schniepp, R.K. Prud'homme, I.A. Aksay, R. Car, *Nano Lett.* 8 (2008) 36–41.
- [42] J. Shen, B. Yan, M. Shi, H. Ma, N. Li, M. Ye, *J. Mater. Chem.* 21 (2011) 3415–3421.
- [43] C. Gómez-Navarro, R.T. Weitz, A.M. Bittner, M. Scolari, A. Mews, M. Burghard, K. Kern, *Nano Lett.* 7 (2007) 3499–3503.
- [44] J.G. Yu, G.P. Dai, Q.J. Xiang, M. Jaroniec, *J. Mater. Chem.* 21 (2011) 1049–1057.
- [45] X. Chen, L. Liu, P.Y. Yu, S.S. Mao, *Science* 331 (2011) 746–750.
- [46] L. Jing, H. Fu, B. Wang, D. Wang, B. Xin, S. Li, J. Sun, *Appl. Catal. B: Environ.* 62 (2006) 282–291.
- [47] C.H. Wang, C.L. Shao, X.T. Zhang, Y.C. Liu, *Inorg. Chem.* 48 (2009) 7261–7268.
- [48] J.K. Park, J.C. Kang, S.Y. Kim, B.H. Son, J.Y. Park, S. Lee, Y.H. Ahn, *J. Phys. Chem. Lett.* 3 (2012) 3632–3638.
- [49] Z.Y. Liu, D.D.L. Sun, P. Guo, J.O. Leckie, *Nano Lett.* 7 (2007) 1081–1085.
- [50] X.L. Yan, T. Ohno, K. Nishijima, R. Abe, B. Ohtani, *Chem. Phys. Lett.* 429 (2006) 606–610.
- [51] B. Ohtani, *J. Photochem. Photobiol. C* 11 (2010) 157–178.
- [52] G. Williams, B. Seger, P.V. Kamat, *ACS Nano* 2 (2008) 1487–1491.
- [53] O. Legrini, E. Oliveros, A.M. Braun, *Chem. Rev.* 93 (1993) 671–698.
- [54] J. Xu, W.Z. Wang, M. Shang, E.P. Gao, Z.J. Zhang, J. Ren, *J. Hazard. Mater.* 196 (2011) 426–430.